Electrochemical diffusion signatures of solid-solution and phase-separating active materials in Li-ion batteries

Journal of Physics: Energy

PAPER

Electrochemical diffusion signatures of solid-solution and phase-separating active materials in Li-ion batteries

Marco Lagnoni and Antonio Bertei*

Department of Civil and Industrial Engineering, University of Pisa, Pisa, Italy
* Author to whom any correspondence should be addressed.

E-mail: antonio.bertei@unipi.it

Keywords: phase-field modelling, GITT, solid-state diffusion, dynamic electrochemical response

Supplementary material for this article is available online

OPEN ACCESS

RECEIVED
25 February 2025

REVISED
2 June 2025

ACCEPTED FOR PUBLICATION
18 June 2025

PUBLISHED
1 July 2025

Abstract

The working principle of lithium-ion batteries lies in the intercalation of lithium ions in electrode active materials, which exhibit either solid-solution or phase-separating behaviour. This study presents a comparative analysis of the electrochemical responses of these two classes of active materials using a multi-particle phase-field model, the structure and description of which are designed to promote easy interpretation by non-modelling experts. Current pulses and open-circuit relaxations, such as those in the galvanostatic intermittent titration technique (GITT), are simulated for different solid-state diffusion coefficients and particle size distributions. The distinct electrode potential responses are explained through the dynamic intra- and inter-particle lithium distributions and their interplay with active material thermodynamics. In solid-solution active materials, numerical results indicate that the solid-state diffusion coefficient tends to be underestimated by the GITT. In phase-separating active materials, current pulses instead generate a shrinking-core lithium distribution along the particle radius (e.g. the Li-rich phase at the particle surface and the Li-poor phase at the particle centre), so that only the phase nucleated at the particle surface can be electrochemically probed in terms of its diffusion and kinetic properties. Such a shrinking-core distribution represents a quasi-equilibrium configuration for a phase-separating active material, resulting in fast electrode potential relaxation upon current interruption and impeding any inter-particle lithium exchange. In fact, while small particles lithiate faster for both active materials during current pulses, the rest phases enable lithium homogenisation among the particles of a solid-solution active material, which can be adequately simulated using a single equivalent particle radius. In contrast, the absence of inter-particle lithium exchange at open circuit in phase-separating active materials may result in over-lithiation of small particles. This poses limitations to single-particle modelling for phase-separating active materials and highlights the need for carefully calibrated rest phases in pulse fast-charging protocols to facilitate inter-particle lithium exchange when the electrode is in an out-of-equilibrium configuration.

Nomenclature

a	characteristic thickness of the interface between Li-poor and Li-rich phases [m]
c_i	molar concentration of intercalated lithium in the ith particle class [mol m^{-3}]
$\tilde{c}_i$	SoL in the ith particle class [-]
$\tilde{c}_{\text{in}}$	initial SoL [-]
c_{max}	maximum concentration of intercalated lithium in the active material [mol m^{-3}]
C_r	C-rate [h^{-1}]
D	solid-state diffusivity [m^2 s^{-1}]
D_{est}	solid-state diffusivity estimated with GITT via equation (11) [m^2 s^{-1}]
E	electrode potential [V]
E_{eq}	electrode equilibrium electric potential evaluated at average SoL [V]
$E_{\text{eq},i}$	equilibrium electric potential in the ith particle class [V]
$E^{\ominus}$	standard equilibrium potential of intercalation in the active material [V]
F	Faraday constant [C mol^{-1}]
j_0	exchange current density of the charge-transfer intercalation reaction [A m^{-2}]
$J_{\text{ct},i}$	charge-transfer current density in the ith particle class [A m^{-2}]
J_{ed}	applied current density per unit of electrode area [A m^{-2}]
J_i	flux of intercalated lithium in the ith particle class expressed as current density [A m^{-2}]
L_{ed}	electrode thickness [m]
n	number of classes of the particle size distribution [-]
Q_{ed}	electrode areal capacity [Ah m^{-2}]
R_g	universal gas constant [J mol^{-1} K^{-1}]
r_i	radial coordinate of the ith particle class [m]
$\tilde{r}_i$	dimensionless radial coordinate of the ith particle class [-]
R_i	radius of the ith particle class [m]
s_i	specific surface area the ith particle class per unit of electrode volume [m^{-1}]
t	time [s]
T	temperature [K]
t_p	duration of the current pulse [s]
t_r	duration of the current relaxation at open-circuit [s]
$\tilde{v}_i$	volumetric composition of the ith particle class in the size distribution [-]

Greek

ΔE_{eq}	change in equilibrium potential upon a current pulse [V]
$\Delta\eta_{\text{sd}}$	change in solid-diffusion overpotential upon a current pulse [V]
ε_{am}	volume fraction of active material within the electrode [-]
$\eta_{\text{ct},i}$	activation overpotential of the charge-transfer intercalation reaction in the ith particle class [V]
η_{ed}	total electrode overpotential [V]
$\eta_{\text{sd},i}$	solid-diffusion overpotential in the ith particle class [V]
μ_i	chemical potential difference of intercalated lithium in the ith particle class [J mol^{-1}]
$\tilde{\mu}_i$	dimensionless chemical potential difference of intercalated lithium in the ith particle class [-]
Ψ	Margules interaction parameter [-]

Subscripts

i	ith particle class

Acronyms

EV	electric vehicle
GITT	galvanostatic intermittent titration technique
LFP	lithium iron phosphate
LIB	lithium-ion battery
NCA	nickel–manganese–aluminium oxide
NMC	nickel–manganese–cobalt oxide
SoL	state-of-lithiation

1. Introduction

Lithium-ion batteries are the electrochemical energy storage systems at the core of the electrification transition, with increasing applications in sectors ranging from portable electronic devices to EVs [1, 2]. The capability of an LIB to store and deliver electric energy stems from the rocking-chair mechanism [3, 4], that is, the intercalation/deintercalation of lithium ions from the electrolyte phase to a host material phase,

conventionally called the active material, at both negative and positive electrodes. Following the charge-transfer intercalation reaction at the electrolyte/active material interface, the active material uptakes lithium ions, thus causing an increase in its SoL, which is a normalised metric of lithium concentration within the active material. Several families of active materials have been developed for various applications: at the positive electrode, NMC [5, 6], NCA [7] and LFP [8, 9] are currently the most used chemistries, while the negative electrode typically features natural or synthetic graphite [10], which can be mixed with silicon or silicon oxide particles [11] to increase the gravimetric capacity [12, 13].

Although there are different ways to classify electrode active materials based on their crystal structure, voltage window and stability, a useful distinction stems from the equilibrium distribution of lithium ions within the active material upon changes in its SoL [14]. In this regard, two distinct behaviours can be distinguished: solid-solution and phase-separating active materials [14, 15]. Solid-solution active materials, such as NMC and NCA, show a homogeneous equilibrium distribution of lithium ions within an active material particle at all SoLs. In this regard, they effectively behave as a solid mixture. Such a solid-solution behaviour produces a monotonously decreasing equilibrium potential as the intercalation proceeds [14]. On the other hand, in phase-separating active materials [16], such as graphite and LFP, there exist one or more ranges of SoL wherein a homogeneous Li distribution is thermodynamically unstable [17, 18]. Such a thermodynamic instability leads to phase separation into regions having Li-rich and Li-poor equilibrium compositions (i.e. high and low equilibrium SoLs), which coexist at open circuit and do not homogenise. Using an analogy, a phase-separating active material behaves as a partially miscible mixture of two phases [19], Li-rich and Li-poor, separated by an interface. Thus, the average SoL of a particle results from the equilibrium SoLs of the Li-rich and Li-poor regions in their relative proportion according to the lever rule. As such, being the lithium chemical potential the same in the two regions, the equilibrium electric potential of a phase-separating active material is constant within the SoL range where phase separation occurs [14, 15].

The description above illustrates a static equilibrium picture of the two active materials. However, there is growing evidence that battery development can be accelerated by understanding the dynamic response of active materials. In fact, characterisation tests, such as GITT [20, 21] and related alternatives [22, 23], rely on dynamic current profiles [24, 25]. In addition, recent investigations show that active materials such as LFP can be activated by current pulses [26], while battery lifetime is positively affected by cycling with dynamic discharge [27]. Thus, the dynamic behaviour of active materials is relevant for practical applications and can differ significantly from their equilibrium configurations. During dynamic operation, concentration gradients are established between the surface and the core of active material particles, leading to lithium-ion redistribution via solid-state diffusion. In electrodes consisting of particles with different particle sizes, fictitious phase separation [28, 29] has been observed during deintercalation in solid-solution active materials as a dynamic artefact driven by electro-autocatalysis [30]. Conversely, the phase separation in LFP nanoparticles can be suppressed during high-rate intercalation [31, 32].

In all of these cases, physics-based modelling has played a major role in understanding the dynamic response of active materials [33, 34]. While battery simulations span from atomistic [35, 36] to system-level approaches [37], the electrochemical signatures of active materials can be conveniently investigated using mean-field models at the particle and electrode levels. Horner *et al* [38] applied single- and multi-particle models to evaluate the diffusion coefficient in solid-solution active materials from GITT, comparing ideal and non-ideal diffusion and accounting for particle size dispersion. Current and voltage pulses have also been simulated for phase-separating active materials [39, 40], whose hysteretic behaviour can be captured by multi-particle modelling [16]. Lai and Ciucci [17] modelled the different concentration profiles and electric behaviour of solid-solution and phase-separating active materials under constant current and constant voltage, later extending the analysis to simulate the electrochemical impedance response [41]. Bazant and co-workers [18, 42] have established consistent theories based on non-equilibrium thermodynamics to simulate the dynamic behaviour of active materials [15], coupling intercalation kinetics [43, 44] with solid-state diffusion [45, 46] and showing consistent validation at the particle level [47, 48].

Despite these excellent achievements, there is a lack of a side-by-side comparison between the fundamental electrochemical signatures of solid-solution and phase-separating active materials under dynamic current profiles, such as during current pulses and resulting relaxations. In fact, the most advanced models incorporate complex intercalation kinetics [42, 43], mechanical strain [31, 49] or electrolyte transport [17], which may blur the basic electrochemical signature due to solid-state diffusion. Hence, in this study, we present a fundamental model tailored to restrict the analysis to the minimum physical and electrochemical phenomena necessary to characterise the distinct behaviour of the two classes of active materials. Such simplicity in the model serves a twofold purpose: on the one hand, it serves to highlight the essential diffusion signatures of battery active materials in dynamic operation; on the other hand, it is intended to facilitate access for experimentalists and beginners to a model-based interpretation of GITT and, more broadly, dynamic battery operation. By presenting simulations with different diffusion coefficient

values and by investigating the effects of particle size distribution, the study offers a comprehensive perspective of active material behaviour. The resulting discussion is relevant for implications on the applicability and interpretation of dynamic electric tests, on the expected active material response to pulsed charge/discharge and the related propensity for degradation phenomena such as lithium plating during fast-charging. Our efforts point towards sounder model-informed planning of experiments for parameter quantification as well as for designing electrodes with optimised characteristics.

The paper is structured as follows. Section 2 illustrates the model along with its assumptions and limitations, keeping the description as simple as possible to emphasise the rationale and stimulate a physical intuition behind the equations. Section 3 describes the model results, starting in section 3.1 from the ideal behaviour of a solid-solution active material during pulsed lithiation, providing a breakdown of its electrochemical response and discussing the accuracy of diffusivity estimation from dynamic electrical tests. Then, in section 3.2, solid-solution and phase-separating active materials are compared side-by-side, linking their electrochemical response to the different lithium distributions driven by solid-state diffusion. Finally, in section 3.3, the role of particle size distribution is investigated, highlighting the practical implications related to how the different distribution of lithium in the two classes of materials may pose risks during the dynamic operation of batteries. Finally, section 4 summarises the key findings of the study.

2. Modelling

In the quest for a simple approach for simulating the dynamic behaviour of solid-solution and phase-separating active materials, we restrict the analysis to a porous electrode versus a Li metal counter-electrode, whose polarisation is assumed to be negligible. It is assumed that the porous electrode is made of spherical particles of an active material, whose particle size distribution can be described by n particle sizes, where R_i denotes the radius of the ith particle class [34, 50]. For the sake of simplicity, isothermal conditions are assumed and no volume expansion/shrinkage of particles upon lithiation/delithiation is considered [50, 51]. Blurring phenomena, such as ionic and electronic transport losses across the ion-conducting electrolyte [52, 53] and the electron-conducting phases [54, 55], respectively, are not accounted for to highlight the electrochemical response of the active material only. Under these premises, all the active material particles experience the same electrode potential, E, across the whole electrode thickness, L_{ed}. The diagram in figure 1(a) serves as a visual guide to the understanding of this section.

Within each particle class i, the distribution of intercalated lithium is modelled according to a microscopic balance, written on an electric charge basis by considering that lithium ions react with one electron upon intercalation, as follows [34, 56]:

$$Fc_{\max}\frac{\partial \tilde{c}_i}{\partial t} + \nabla \cdot J_i = Fc_{\max}\frac{\partial \tilde{c}_i}{\partial t} + \frac{1}{r_i^2}\frac{\partial}{\partial r_i}\left(r_i^2 J_i\right) = 0 \tag{1}$$

where F is the Faraday constant, t is time, r_i is the radial coordinate and $c_{\max}$ is the maximum molar concentration of intercalated lithium that the active material can store at full lithiation. The latter defines the SoL of each particle, $\tilde{c}_i$, as the ratio between the molar concentration of intercalated lithium, c_i, and the maximum concentration, that is, $\tilde{c}_i = c_i/c_{\max}$ [14]. A dimensionless radial coordinate, $\tilde{r}_i = r_i/R_i$, can also be introduced. The balance in equation (1) accounts for both the accumulation of intercalated lithium (i.e. the time-derivative term) and its transport across the particle radius (i.e. the divergence term), where the latter is explicitly framed in spherical coordinates in the middle part of the equation [50].

In equation (1) the variable J_i denotes the flux of intercalated lithium across the particle radius, expressed as current density. Since the active material can be treated as a lattice of filled and empty sites with molar fractions $\tilde{c}_i$ and $1-\tilde{c}_i$ [14, 17], respectively, the transport of intercalated lithium is governed by solid-state diffusion. According to non-equilibrium thermodynamics [38, 42], such a diffusion flux can be expressed as [14, 57]:

$$J_i = -FDc_{\max}\tilde{c}_i\left(1-\tilde{c}_i\right)\nabla\tilde{\mu}_i \tag{2}$$

where D is the solid-state diffusion coefficient and $\tilde{\mu}_i = \mu_i/\left(R_g T\right)$ is the dimensionless form of the chemical potential difference μ_i, i.e. the difference between the chemical potential of filled and empty active material sites [14], where R_g is the universal gas constant and T is the absolute temperature.

The chemical potential difference μ_i is calculated as the variational derivative of the Gibbs free energy of the active material, whose definition is left to specific studies [42, 44]. For the purposes of the present investigation, it suffices to mention that the Gibbs free energy is modelled by treating the active material as a non-ideal mixture of filled and empty sites [14, 35], accounting for bulk and surface area contributions to

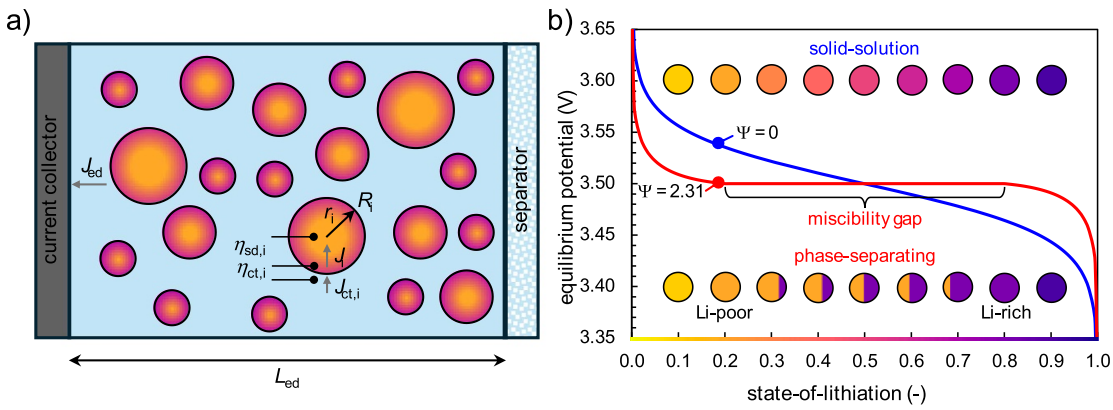

Figure 1. (a) Schematic representation of the modelled electrode, with indications of different particle sizes, electrode current density, as well as charge-transfer and intercalation fluxes with corresponding overpotentials. (b) Equilibrium potential as a function of state-of-lithiation for solid-solution (blue) and phase-separating (red) active materials. The insets show the qualitative distribution of intercalated lithium in a particle at equilibrium, with the colourmap of state-of-lithiation superimposed on the abscissa.

the free energy functional. In this regard, the Gibbs free energy is made of a thermodynamic contribution plus, in the case of phase separation in Li-rich and Li-poor phases, a non-local term [57], which accounts for the free energy of interfaces [42] according to a Cahn–Hilliard phase-field framework [58, 59].

The regular solution model [17, 60] arguably represents the simplest approach to account for deviations from ideal behaviour, including phase separation. In this mean-field model, the excess free energy is regulated by a single factor, called Margules (or Flory–Huggins) parameter, Ψ, that encodes the enthalpic interactions between filled and empty sites, which are attractive for $\Psi < 0$ and repulsive for $\Psi > 0$ [19]. In particular, setting $\Psi > 2$ generates a miscibility gap in the Gibbs free energy functional, leading to phase separation in Li-rich and Li-poor phases, with equilibrium compositions symmetric with respect to $\tilde{c}_i = 1/2$ (see figure 1(b)). Following this approach, the dimensionless chemical potential difference is given by [19, 61]:

$$\tilde{\mu}_i = \ln\left(\frac{\tilde{c}_i}{1-\tilde{c}_i}\right) + \Psi\,(1-2\tilde{c}_i) - a^2\nabla^2\tilde{c}_i \tag{3}$$

where the first term represents the entropic term of the thermodynamic contribution to the free energy, the second term is the excess enthalpic contribution, while the third non-local term is present only for phase-separating active materials (i.e. for $\Psi > 2$) to account for the surface tension energy stored at the interface between Li-rich and Li-poor phases, with a being its characteristic thickness. It is worth noting that, in the ideal case of $\Psi = 0$ (i.e. in the absence of phase separation), plugging equation (3) in equation (2) reduces the flux expression to Fick diffusion law (i.e. $J_i = -FD\nabla c_i$), as it should be [14, 39].

The dimensionless chemical potential difference in equation (3) dictates not only the solid-state diffusion, but also the charge-transfer kinetics of lithium intercalation [42]. In fact, for each particle class, the equilibrium electric potential $E_{eq,i}$ follows from Nernst law as [44]:

$$E_{eq,i} = E^{\Theta} - \frac{R_g T}{F}\tilde{\mu}_i \tag{4}$$

where E^{Θ} is the standard electric potential of intercalation in the active material. Figure 1(b) reports the equilibrium potential of solid-solution and phase-separating active materials according to equation (4), while the insets qualitatively reproduce the equilibrium SoL distribution within a particle in the two scenarios. When evaluated at the particle surface (i.e. at $r_i = R_i$ or, equivalently, at $\tilde{r}_i = 1$), the equilibrium potential takes part in the activation overpotential of the charge-transfer reaction of Li intercalation, $\eta_{ct,i}$, as [62]:

$$\eta_{ct,i} = E - E_{eq,i}|_{r_i=R_i}. \tag{5}$$

In order not to mask the diffusion signature of the active material, we can assume a simple linear relationship between the activation overpotential and the charge-transfer current density $J_{ct,i}$ at the particle surface, such as:

$$J_{ct,i} = j_0\frac{F}{R_g T}\eta_{ct,i} \tag{6}$$

where j_0 is the exchange current density [42, 62]. It is worth noting that even complex electrokinetic expressions, such as Butler–Volmer [62, 63], Marcus [42] or coupled ion-electron transfer [64, 65], reduce to the linear form in equation (6) for relatively small activation overpotentials. The charge-transfer rate in equation (6) acts as a boundary condition for the balance in equation (1), since it matches the intercalated lithium flux at particle surface ($J_i|_{r_i=R_i} = J_{ct,i}$), while the diffusion flux is nil at the particle centre for symmetry (i.e. $J_i|_{r_i=0} = 0$).

The current densities transferred at the particles surface, $J_{\mathrm{ct},i}$, must satisfy a total current balance [34, 50]:

$$\sum_{i=1}^{n} J_{\mathrm{ct},i} s_i L_{\mathrm{ed}} = J_{\mathrm{ed}} \tag{7}$$

where J_{ed} is the applied current density per unit of electrode area. Equation (7) states that the current applied to the electrode is distributed among the particles according to their surface areas, thus determining the charge-transfer rates $J_{\mathrm{ct},i}$ and, in turn, the lithium distribution within each particle. In particular, $s_i = 3\varepsilon_{\mathrm{am}}\tilde{\nu}_i/R_i$ is the specific surface area per unit of electrode volume of the ith particle class, where $\varepsilon_{\mathrm{am}}$ is the volume fraction of active material in the electrode and $\tilde{\nu}_i$ is the fraction of particles (in volume basis) having radius R_i in the particle size distribution. The applied current density J_{ed} can also be related to the C-rate $C_r = |J_{\mathrm{ed}}|/Q_{\mathrm{ed}}$, where Q_{ed} is the electrode areal capacity:

$$Q_{\mathrm{ed}} = F\varepsilon_{\mathrm{am}} c_{\max} L_{\mathrm{ed}}. \tag{8}$$

Hence, the set of equations (1)–(8) defines a multi-particle model encompassing the minimum relevant physics necessary to investigate the electrochemical signature of different active materials. By starting from a uniform SoL across all the particles (i.e. $\tilde{c}_i = \tilde{c}_{in}$ for $i = 1, \ldots, n$), the model can be solved to mimic a porous electrode subject to different dynamic galvanostatic conditions, such as current pulses interspersed by relaxation phases. The model is particularly effective to decouple, for each particle, the charge-transfer and solid-diffusion contributions to the total electrode overpotential η_{ed} that, making use of equation (5), is defined as:

$$\eta_{\mathrm{ed}} = E - E_{\mathrm{eq}} = \eta_{\mathrm{ct},i} + \eta_{\mathrm{sd},i} \tag{9}$$

where $\eta_{\mathrm{sd},i} = E_{\mathrm{eq},i}|_{r_i=R_i} - E_{\mathrm{eq}}$ is the solid-diffusion overpotential of the ith particle class and E_{eq} is the electrode equilibrium potential evaluated according to equation (4) at average electrode SoL.

The model is solved in Comsol Multiphysics® v. 6.2 according to the base-case parameters listed in table 1. The parameters are not tailored to reproduce any specific Li-ion battery application but, rather, they are meant to be representative of generic classes of active materials. The electrode areal capacity is set to 20 Ah m^{-2} that, according to an active material volume fraction of 50% and a maximum storage concentration of intercalated lithium of 30 000 mol m^{-3}, corresponds to an electrode thickness L_{ed} of ca. 50 μm. In the base-case scenario, all the particles are assumed to have the same radius of 5 μm; nevertheless, a distribution of particle sizes is also considered in section 3.3. An ideal solid-solution active material is modelled by setting $\Psi = 0$, while a representative phase-separating active material is modelled with $\Psi = 2.31$ [39]; for the latter, the equilibrium compositions of the Li-poor and Li-rich phases are at $\tilde{c} = 0.20$ and $\tilde{c} = 0.80$, respectively, as also denoted by the voltage plateau in figure 1(b). This SoL range is similar to that of LFP [66], although slightly narrower. The sharp interface transition between Li-poor and Li-rich phases is reproduced by $a = 50$ nm. For both solid-solution and phase-separating active materials, the standard electric potential is set at $E^{\ominus} = 3.5$ V vs Li metal. This value is just an arbitrary potential constant with no significant impact on model results, so any type of positive or negative electrode active material can be represented by shifting $E^{\ominus}$ accordingly. The value of the exchange current density j_0 is purposely chosen to produce an activation overpotential drop of 20 mV at 1C in the selected conditions. The diffusivity D lies in the typical range reported for NCA [21] and the NMC class [67, 68], while a sensitivity analysis is reported in section 3.1 to encompass a wider range of materials. Starting from 10% SoL for both active materials, 1C current pulses are simulated to increase the average SoL by 10% in $t_p = 6$ min followed by a relaxation at open-circuit for $t_r = 14$ min. This relaxation time is sufficient under the present conditions to allow the system to reach near-complete equilibrium before the start of the next current pulse. Although longer open-circuit relaxation times are typically adopted in GITT protocols (e.g. 1–2 h) [40], extending the relaxation time further would not influence the simulation results.

While the model is meant to highlight the electrochemical diffusion signatures of solid-solution and phase-separating active materials, its simplicity inevitably introduces some limitations. First, spherical symmetry is assumed for all the particles while battery electrodes may be made by secondary particles of different shapes [69, 70]. Along with the linear kinetic simplification (equation (6)), which excludes

Table 1. Model parameters.

Parameter	Value	Parameter	Value
Q_{ed}	20 Ah m^{-2}	ε_{am}	0.50
c_{max}	30 000 mol m^{-3}	R	5 μm
E^{Θ}	3.5 V	Ψ	0 (solid-solution) 2.31 (phase-separating)
D	10^{-14} m^2 s^{-1}	j_0	1.7205 A m^{-2}
a	50 nm	T	298 K
$\tilde{c}_{in}$	0.10	C_r	1 h^{-1}

kinetic-diffusion couplings capable of explaining auto-catalytic effects [45] giving rise to suppression or fictitious phase separation [30, 71], the assumed spherical symmetry cannot reproduce the intercalation wave propagation in phase-separating materials for low current densities [61, 72]. Since electrolyte losses are neglected, the through-thickness heterogeneous intercalation distribution in thick electrodes cannot be reproduced. No particle volumetric expansion [51, 73] and no mechanical energy or anisotropy in the chemical potential [31, 49] are considered by the current regular solution theory (equation (3)), making the model arguably inaccurate for active materials such as silicon or $LiFePO_4$, respectively. Finally, the model does not include any degradation process such as particle fracture [74, 75], growth of solid electrolyte interphase [76, 77] or lithium plating [78, 79]. Obviously, all these phenomena can be accounted for by adding the relevant physics to the framework: while this would improve model accuracy for some specific applications, the general features of active material electrochemical behaviour can still be captured by the minimum set of physical-chemical processes reproduced by the simplified model [17, 39].

3. Results and discussion

3.1. Ideal solid-solution active material

The simplest dynamic current profile is arguably a current pulse followed by a rest period at an open circuit [22, 80], which can be regarded as the building element of more complex dynamic profiles [81, 82]. A series of current pulses, meant to increase the SoL of the active material by a fixed amount, interspersed by relaxation phases, is usually referred to as a GITT [20, 83]. Thus, in this study, the GITT is used as a convenient platform to investigate the dynamic response of active materials. We begin by considering the response of a porous electrode made by uniform particles with radius $R = 5$ μm of an ideal solid-solution active material. The interaction parameter is set to $\Psi = 0$ with $a = 0$, so that solid-state diffusion in equation (2) follows Fick's law (i.e. $J = -FD\nabla c$) and the equilibrium electric potential in equation (4) reduces to the Nernst equation of an ideal lattice material [14, 84]:

$$E_{eq} = E^{\Theta} - \frac{R_g T}{F} \ln\left(\frac{\tilde{c}}{1-\tilde{c}}\right). \tag{10}$$

The other simulation parameters are reported in table 1.

Figure 2 summarises the electrochemical response of a solid-solution active material during the GITT. Figure 2(a) shows that current pulses at 1C for $t_p = 6$ min (purple, right axis) cause an increase in SoL by 10% per pulse (red, right axis), which remains constant during the relaxation phases which last $t_r = 14$ min. In particular, eight current pulses, sequentially numbered in the figure, are applied, changing the SoL from $\tilde{c}_{in} = 0.1$ to $\tilde{c} = 0.9$. The corresponding voltage response is shown on the left axis. The blue line represents the electrode potential E, which decreases during the current pulse as a consequence of activation and diffusion overpotentials; during the open-circuit phases the electrode potential relaxes, gradually attaining the equilibrium potential E_{eq}, represented by the dashed green line and calculated according to equation (10) with the average electrode SoL.

A convenient way to compare the electrochemical response at all the pulses is shown in figure 2(b), which collects the electrode potential by shifting the voltage to 3.50 V at the start of each pulse. The figure highlights that the activation overpotential, η_{ct}, can be easily identified as the potential drop as soon as the current is applied at $t = 0$ or, equivalently, as the instantaneous potential rise at current removal at $t = 6$ min [20, 85]. In this specific case, since the intercalation current follows linear kinetics independent of the SoL (equation (6)), the activation overpotential η_{ct} is the same for all the pulses. Conversely, the electrode potential, albeit shifted, does not collapse on a single master curve. In particular, the shifted voltage reaches a minimum at the end of the current pulse (i.e. at $t = 6$ min), whose value first increases with the pulses and then decreases from pulse 5 to pulse 8. Accordingly, the voltage relaxation after current interruption spans a wider potential window for the pulses at the extremes of the SoL range (e.g. pulses 1 and 8) compared to the

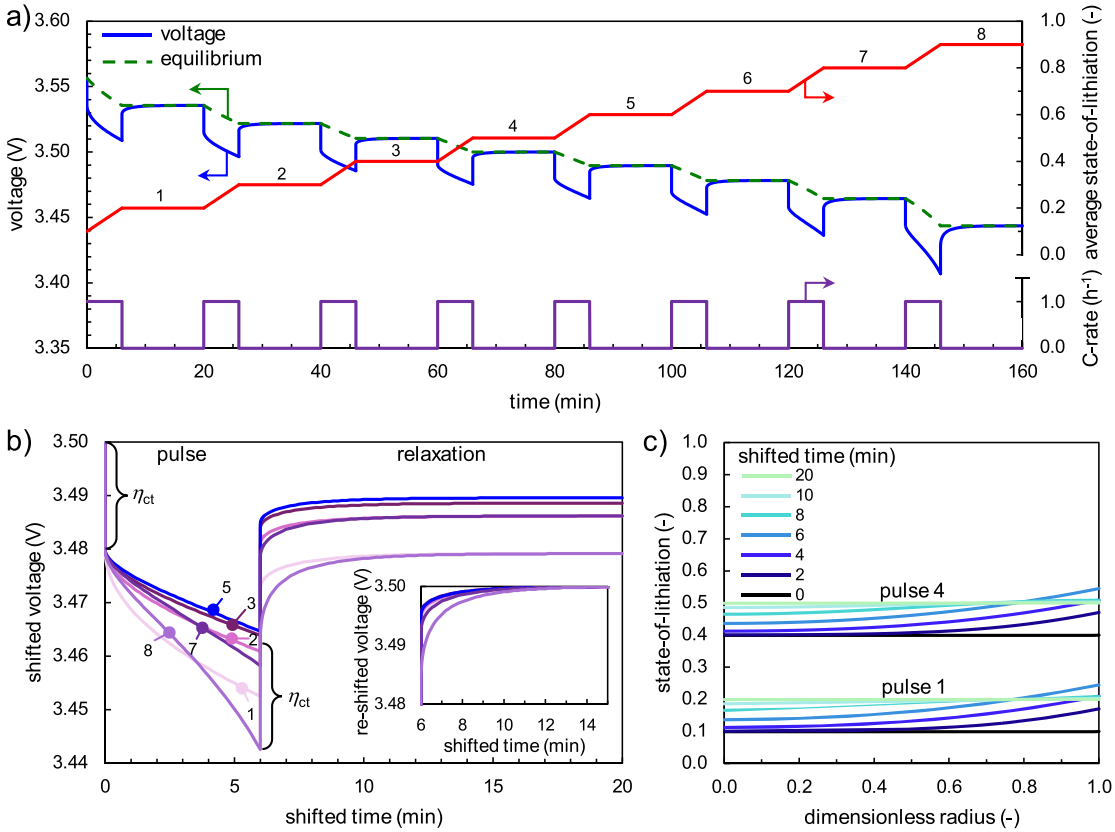

Figure 2. Phenomenology of the electrochemical response of a solid-solution active material, with parameters listed in table 1, during a GITT. (a) Electrode (blue) and equilibrium (green) potentials (left axis) as a function of time, along with the applied current (purple, lower right axis) and corresponding state-of-lithiation (red, upper right axis). Each pulse is numbered from 1 to 8. (b) Voltage response versus time shifted to align the starting electrode potential at 3.50 V for selected pulses; the inset reports the relaxation voltage re-shifted to align the final electrode potential at 3.50 V. (c) SoL distribution along the dimensionless radius of the particle for different times during pulses number 1 and 4.

central ones (e.g. pulses 3 and 5). This is also visualised in the inset of figure 2(b), where the voltage response is re-shifted to align the potential at the end of relaxation at 3.50 V for all the pulses.

The reason for the different potential values among the pulses, regardless of the shifting strategy, lies in the SoL at the particle surface, $\tilde{c}|_{r=R}$. According to equation (5), the electrode potential E follows directly from the sum of the activation overpotential η_{ct}, which is constant as previously discussed, and the equilibrium potential at particle surface $E_{eq}|_{r=R}$, which depends on the SoL at particle surface $\tilde{c}|_{r=R}$ via equation (10). Figure 2(c) shows that the SoL increases during the current pulse (i.e. from $t = 0$ to $t = 6$ min), being maximum at the particle surface (i.e. at $\tilde{r} = 1$) where lithiation occurs, gradually penetrating the particle via solid-state diffusion; during relaxation (i.e. from $t = 6$ min to $t = 20$ min), lithium concentration homogenises within the particle (see also the insets in figure 1(b)). Notably, given the linear intercalation kinetics (equation (6)) and the Fick diffusion law, the intercalated lithium distribution is exactly the same for all the pulses (compare pulse 1 with pulse 4 in figure 2(c)), being only shifted by an additive constant equal to the SoL at the start of the current pulse. Thus, the voltage response is dictated by how sensitive the equilibrium potential is to surface SoL $\tilde{c}|_{r=R}$ according to equation (10). As shown in figure 1(b), the equilibrium potential of an ideal solid-solution material (in blue) is increasingly sensitive to changes in SoL as $\tilde{c}$ deviates from 0.5, with maximum change in E_{eq} as $\tilde{c}$ approaches 0 or 1. Mathematically, the derivative $\partial E_{eq}/\partial\tilde{c}$ is symmetric to $\tilde{c} = 0.5$ where $\partial E_{eq}/\partial\tilde{c}$ shows a minimum. Therefore, although the difference between surface and average SoL is the same for all the pulses as in figure 2(c), the larger sensitivity of the equilibrium potential to the surface lithium concentration explains the wider voltage span in figure 2(b) for pulses at the extremes of the SoL range (e.g. pulses 1 and 8). From a different perspective, while the dynamics of intercalated lithium distribution is the same for all the pulses except for an additive constant (figure 2(c)), the different sensitivity of the thermodynamic relationship between electric potential and SoL affects the spread of the electrochemical response in figure 2(b).

This observation directly inspires the question of how different diffusivity values may affect the electrochemical response. Such an investigation is reported in figure 3(a) for pulse 4 (i.e. from $\tilde{c} = 0.4$ to $\tilde{c} = 0.5$) and repeated in the inset for pulse 8 (i.e. from $\tilde{c} = 0.8$ to $\tilde{c} = 0.9$), by allowing a longer relaxation

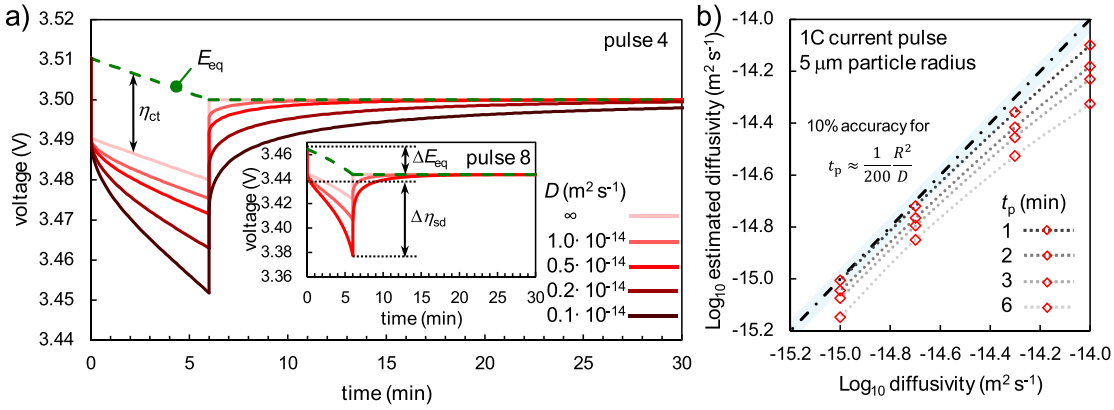

Figure 3. (a) Electrode potential as a function of time for a solid-solution active material with different diffusivity values for two representative pulses (pulse 4 in main graph, pulse 8 in the inset). Model parameters are in table 1, with an increased relaxation time $t_r = 1$ h. (b) Accuracy of diffusivity estimation according to Weppner and Huggins method [20] as a function of diffusivity values for different durations of the current pulse (data generated with pulse 4). The pale shaded area identifies a region within 10% accuracy.

time, $t_r = 1$ h, to capture the voltage response of sluggish lithium diffusion. Figure 3(a) shows that, in the case of infinitely fast diffusion (light pink), the electrode potential would simply reproduce the equilibrium potential response, shifted by the activation overpotential. In fact, an infinite solid-state diffusivity would produce a uniform lithium concentration across the particle radius, with no sensible gradient between the particle surface and the particle core. As such, the voltage relaxation upon current interruption is instantaneous because the lithium distribution within the particle is always equilibrated with the applied current condition. As the diffusivity D decreases (darker scale of red in figure 3(a)), the electrode potential progressively decreases as a consequence of the increased magnitude of the diffusion overpotential η_{sd}, as introduced in equation (9). In fact, slower diffusion leads to a steeper concentration gradient at the particle surface compared to the average electrode SoL, thus increasing the magnitude of η_{sd}. This is exacerbated when the current pulse probes an SoL range where the equilibrium potential is more sensitive to $\tilde{c}$: in fact, for $D = 0.5 \cdot 10^{-14}$ m^2 s^{-1} (bright red in figure 3(a)), there is comparatively a deeper minimum in electrode potential for pulse 8 ($E = 3.378$ V as in the inset of figure 3(a), corresponding to $|\eta_{ed}| = 66$ mV) than for pulse 4 ($E = 3.412$ V as in the main graph of figure 3(a), corresponding to $|\eta_{ed}| = 28$ mV).

Figure 3(a) also reports the changes in equilibrium potential, ΔE_{eq}, and diffusion overpotential, $\Delta \eta_{sd}$, which are used in the Weppner and Huggins method [20] to estimate the material diffusivity, D_{est}, that, for an electrode made by monosized spherical particles of radius R, reads as follows:

$$D_{est} = \frac{4}{\pi t_p}\left(\frac{R}{3}\right)^2\left(\frac{\Delta E_{eq}}{\Delta \eta_{sd}}\right)^2. \tag{11}$$

In addition to the Weppner and Huggins seminal paper [20], many studies have investigated the accuracy of equation (11) and provided with guidelines on how to design a proper GITT [23, 38], including the removal of intercalation kinetics responses [85] and applications to phase-separating active materials [40, 86]. Among the many conditions that need to be met, there is a critical prerequisite that deserves careful attention: the pulse duration t_p must be much smaller than the characteristic diffusion time R^2/D [20]. Such a prerequisite ensures that, during the current pulse, the intercalated lithium penetrates only the external fraction of the particle radius, without the centre of the particle being affected. As already shown in figure 2(c), a 6 min pulse is too long for the conditions simulated in this study, since the gradient in lithium concentration extends down to $r = 0$ already after 4 min. Figure 3(b) reports in a parity plot how short the pulse duration must be to achieve 10% accuracy (denoted by a pale shaded area) in the estimation of solid-state diffusivity. Numerical results indicate that equation (11) tends to underestimate the diffusivity and that comparatively shorter pulse durations are required as the diffusivity increases. As a rule of thumb, for the conditions analysed in this study, 10% accuracy is achieved when the current pulse lasts less than one two-hundredth of the characteristic diffusion time, as embedded in the figure. Such a short pulse duration implies that the potential drops ΔE_{eq} and $\Delta \eta_{sd}$ may become too small to be accurately distinguished from other sources of overpotential and from measurement noise [40, 85]. For these reasons, a careful design of GITT is required [24, 40] and the estimation of active material diffusivity can be complemented by more sensitive approaches [22, 38] and cross-validation methods [23, 25].

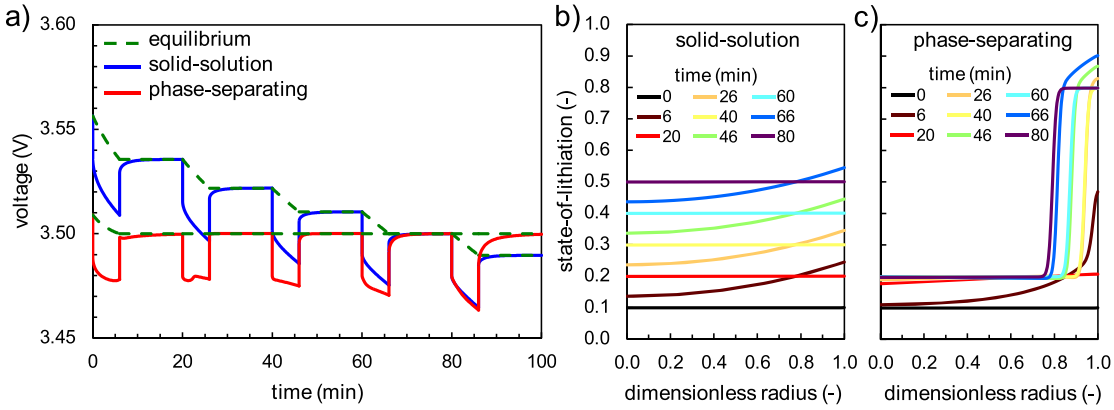

Figure 4. Comparison between the dynamic response of solid-solution and phase-separating active materials, with parameters listed in table 1. (a) Electrode potential of the two materials during a GITT virtual experiment. SoL distribution along the dimensionless radius of the particle at selected times (start and end of current pulses) for (b) solid-solution, (c) phase-separating active materials.

3.2. Phase-separating active material

The dynamic responses of solid-solution and phase-separating active materials during pulsed lithiation are compared in figure 4. The same parameters, listed in table 1, are used for both materials, except for their different thermodynamics (figure 1(b)). Figure 4(a) reports the electrode and equilibrium potentials of the active materials during the virtual GITT experiments, while figures 4(b) and (c) show the distribution of SoL across particle radius at selected times. Animated simulations of the intercalated lithium distribution in the two active materials are displayed in supplementary videos S1 and S2.

The electrochemical response of a solid-solution material (in blue in figure 4(a)), consisting of electric potential drops followed by smooth relaxations towards equilibrium, has already been discussed in the previous section. This matches the SoL distribution in figure 4(b): a concentration gradient is established at the end of each current pulse ($t = 6,\ 26,\ 46,\ 66$ min), followed by the achievement of a uniform lithium distribution at the end of relaxation ($t = 20,\ 40,\ 60,\ 80$ min). Such a pattern is repetitive, pulse after pulse. On the other hand, the phase-separating active material shows distinct features which deserve proper analysis.

The first current pulse, which increases the average SoL from $\tilde{c} = 0.1$ to $\tilde{c} = 0.2$, activates phase separation at the particle surface, as evidenced by the SoL distribution at $t = 6$ min in figure 4(c). In fact, the surface concentration $\tilde{c}|_{r=R}$ overshoots $\tilde{c} = 0.2$, entering the miscibility gap, i.e. the range between equilibrium compositions $\tilde{c} = 0.2$ and $\tilde{c} = 0.8$ where the active material phase-separates in Li-rich and Li-poor phases (see figure 1(b)). However, since the average composition, equal to $\tilde{c} = 0.2$, lies just outside the miscibility gap, after current interruption the intercalated lithium spreads rather homogeneously across the particle (red curve at $t = 20$ min in figure 4(c)). The corresponding electrode potential in figure 4(a) (red curve) experiences a fast rise towards equilibrium, with a minimal voltage dip between $t = 6$ min and $t = 20$ min.

The second current pulse, starting at $t = 20$ min, increases the particle average SoL by up to 30%, which lies within the thermodynamically unstable region of the active material. Figure 4(c) (orange curve at $t = 26$ min, which is partly hidden by the yellow curve) clearly shows that phase separation takes place: at the particle surface lithium concentration goes beyond the Li-rich equilibrium composition (i.e. $\tilde{c}|_{r=R} > 0.8$) and a sharp interface, denoted by a steep concentration gradient, separates the Li-rich phase close to the particle surface from the Li-poor composition ($\tilde{c} = 0.2$) at the core of the particle. The transition at the particle surface of the Li-rich/Li-poor interface, with its excess surface tension energy, perturbs the electrode potential, which shows a small hump at ca. 23 min (figure 4(a), see also video S2). As the current is interrupted, the lithium concentration gradient quickly relaxes (compare the orange and yellow curves at $t = 26$ min and $t = 40$ min, respectively, in figure 4(c)), as better evidenced by video S2. Such a rapid smoothing of the lithium concentration gradient at the particle surface is responsible for the almost instantaneous voltage relaxation of the phase-separating active material upon current removal, much sharper than for the solid-solution active material (compare red and blue curves in figure 4(a) at $t = 26$ min). The equilibrium distributions of intercalated lithium after the second pulse (i.e. at 30% average SoL) are remarkably different between the two materials: a uniform distribution at $\tilde{c} = 0.3$ for the solid-solution material versus a shrinking-core distribution [72, 87], with Li-rich phase ($\tilde{c} = 0.8$) at the surface and Li-poor phase ($\tilde{c} = 0.2$) in the core of the particle, for the phase-separating material (yellow curves at $t = 40$ min for figures 4(b) and (c), respectively).

Once the separation in Li-rich and Li-poor phases is established, the next current pulses only shift the interface inwards as more lithium is intercalated in the particle. Figure 4(c) shows that, at the end of the third current pulse ($t = 46$ min, green curve), the Li-rich phase encompasses a larger portion of the particle. There is a tiny concentration gradient at the surface that produces a decreasing electrode potential during the current pulse (red curve in figure 4(a) between $t = 40$ min and $t = 46$ min); since just a tiny portion of the particle is out-of-equilibrium (i.e. with $\tilde{c} > 0.8$), solid-state diffusion ensures a rapid relaxation towards equilibrium (light blue curve at $t = 60$ min in figure 4(c)), which is also evidenced by the fast electrode potential rise at $t = 46$ min in figure 4(a). The subsequent current pulses repeat the same pattern; however, as a larger portion of the particle gets engulfed by the Li-rich phase, and more extended concentration gradients are established at the particle surface (see the blue line at $t = 66$ min in figure 4(c)), the relaxation dynamics becomes incrementally slower given the longer diffusion distance across the particle radius. This behaviour is confirmed experimentally, for example in graphite, which shows two miscibility gaps (namely, one between stage 3 and stage 2 and one between stage 2 and stage 1): for both of them, as reported by Ahn *et al* [65] (see, in particular, their supplementary figure S4), the relaxation dynamics of the electric potential is comparatively slower as phase separation progresses. As a consequence, the electrode potential response of the phase-separating active material during current pulses and relaxations becomes progressively similar to that of the solid-solution active material as the particle SoL increases (compare red and blue curves beyond $t = 60$ min in figure 4(a)).

Having compared the dynamic responses of solid-solution and phase-separating active materials, it is worth investigating how a change in solid-state diffusivity may affect the dynamics of the latter. Figure 5 compares three case studies: the first one (solid red line) considers a constant diffusivity $D = 10^{-14}$ m^2 s^{-1} across the whole SoL range, as a base-case scenario; the second one (dashed purple line) assumes halved diffusivity for the Li-rich phase only (i.e. $D = 0.5 \cdot 10^{-14}$ m^2 s^{-1} for $\tilde{c} > 0.5$); in the third case (dotted black line) the diffusivity is halved in the whole SoL range. The dynamic distribution of intercalated lithium across the particle radius in the three cases is shown in videos S2, S3, and S4, respectively. Numerical results show that during the first pulse and relaxation (i.e. for $t \leqslant 20$ min) there is no difference between the first and second cases (red and purple, respectively) in terms of electrode potential (figure 5(a)) because the Li-rich phase has not fully nucleated yet at the particle surface (see figure 5(b) at $t = 6$ min). Instead, in the third case, a shorter penetration of lithium intercalation, with a corresponding steeper concentration gradient, occurs due to the slower solid-state diffusion (dotted black line in figure 5(b) at $t = 6$ min), causing a minor deviation in electric potential response during the first pulse (figure 5(a)). Rather similar considerations apply to the second pulse, during which phase separation is activated by nucleation of a thin layer of Li-rich phase at the particle surface (figure 5(b), $t = 26$ min). A more prominent deviation is highlighted from the third pulse onward, that is, from $t \geqslant 40$ min. Since the Li-rich phase has already nucleated at the particle surface, its diffusion properties dictate the dynamics of the active material during current pulses and relaxations. As shown in figure 5(b) at $t = 46$ min, there is no difference in lithium distribution between the second case (halved D for Li-rich phase only, dashed purple curve) and the third case (halved D for both phases, dotted black curve) because, in a shrinking-core intercalation mechanism, it is the Li-rich phase exposed at the particle surface that dictates the interface movement, while the Li-poor phase is confined at the particle centre and plays no role in intercalation dynamics. Notably, only the potential of the Li-rich phase is electrochemically probed. Thus, from the third pulse onward, via the voltage response we can only distinguish between the first case (i.e. constant diffusivity $D = 10^{-14}$ m^2 s^{-1}, solid red curve) and the other two cases with reduced Li-rich phase diffusivity (purple and black curves), whose responses overlap. In other words, in a GITT experiment featuring lithiation current pulses, only the Li-rich phase diffusivity can be probed since the Li-poor phase at the particle centre never gets exposed to the electrochemical signal. Intuitively, the diffusivity of the Li-poor phase can be probed by performing a GITT in delithiation mode because, in such a case, the Li-poor phase will nucleate at the particle surface.

In summary, in a phase-separating active material, the diffusivity of the phase that nucleates at the particle surface dictates the dynamics of interface movement upon lithiation/delithiation and, in turn, the electric potential response. The Weppner and Huggins method [20], as for equation (11), obviously cannot be applied at it stands within the miscibility gap; in fact, there is no diffusivity associated with a SoL between the Li-poor and Li-rich compositions because such a uniform composition is thermodynamically unstable [14]. The electrochemical response of a phase-separating active material at compositions between the miscibility gap is, rather, the convolution of the kinetic properties of the phase nucleated at the particle surface along with the movement of the Li-poor/Li-rich interface, which is driven by surface tension effects in a strong interplay with particle morphology (e.g. particle shape, distribution of primary particles, crystal orientation, etc). Hence, proper physics-based modelling [39, 65] is required to go beyond the classical analytical solutions such as equation (11), based on Fick diffusion, and thus extract the diffusion properties of phase-separating active materials.

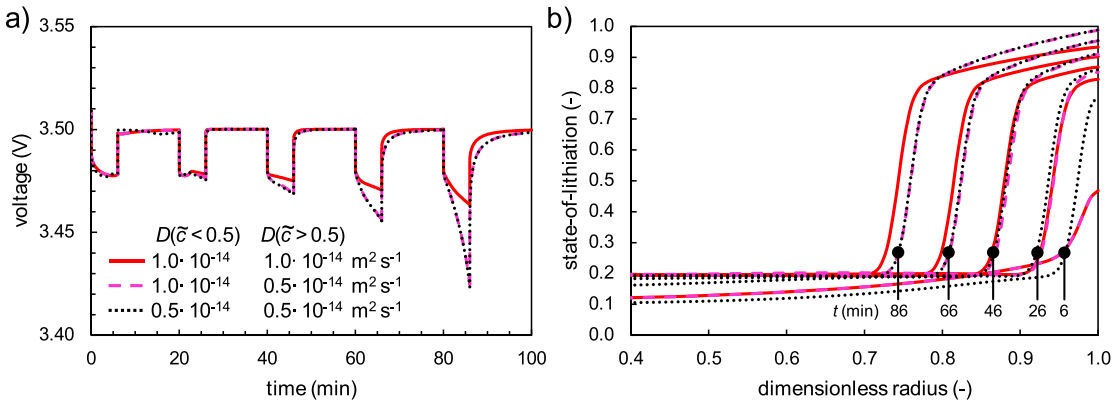

Figure 5. Effect of solid-state diffusivity in the dynamic response of a phase-separating active material during a GITT virtual experiment. (a) Electrode potential as a function of time during current pulses and relaxations. (b) SoL distribution along the dimensionless radius of the particle at the end of current pulses. Three cases are considered: uniform diffusivity in the whole SoL range (solid red line), halved diffusivity for the Li-rich phase (i.e. for $\tilde{c} > 0.5$, dashed purple line), halved diffusivity in the whole SoL range (dotted black line).

3.3. Particle size distribution

So far, the electrochemical signature of a single representative particle in an active material has been investigated; however, battery electrodes are made of many particles. We shall anticipate that, even when no external current is applied, the active material in a multi-particle system experiences the transfer of intercalated lithium among different particles when the latter are in out-of-equilibrium conditions. Such inter-particle lithium transfer is mediated by the electrolyte. Should finite ionic conductivity and diffusivity be considered, the buildup of concentration and ionic potential gradients in the electrolyte would contribute with their overpotential loss to the electrode response. Instead, in our model, lithium-ion transport in the electrolyte phase is assumed to be infinitely fast, resulting in a direct ionic connection between particles of different sizes in the electrode (regardless of their location) without generating any electrolyte resistance that may blur the electrochemical signatures of active materials during such inter-particle exchange of lithium. In the following, a simplified particle size distribution is considered: three particle sizes (namely, $R_1 = 3$ μm, $R_2 = 5$ μm and $R_3 = 7$ μm) are modelled by enforcing a symmetric volumetric composition ($\tilde{\nu}_1 = 0.1$, $\tilde{\nu}_2 = 0.8$, $\tilde{\nu}_3 = 0.1$, denoted as 10/80/10%) so that the volume-average particle radius is $R = 5$ μm as for the monosized case.

Let us repeat the virtual experiment as in figure 4(a), with 1C current pulses lasting 6 min interspersed with open-circuit phases of 14 min. Before addressing the electric potential response, which is observable at battery terminals, it is worth discussing the dynamic lithium distribution among the particles, as shown in figure 6 for both solid-solution and phase-separating active materials. The corresponding animations are displayed in supplementary videos S5 and S6. Starting from the solid-solution material (figure 6(a)), the plot at $t = 6$ min, which corresponds to the end of the first current pulse (from 10% to 20% average SoL), highlights that small particles ($R_1 = 3$ μm, solid line) have experienced more lithium intercalation than larger particles ($R_3 = 7$ μm, dotted line) during the current pulse. Such a behaviour can be easily explained by considering that small particles have a larger surface-to-volume ratio, so they get comparatively more exposed to intercalation per unit volume than larger particles. At the end of the current pulse, the particles are in an out-of-equilibrium configuration: intercalated lithium has a higher chemical potential in small particles due to its larger concentration (especially at the particle surface, i.e. at $\tilde{r}_1 = 1$), while the lithium chemical potential is smaller in the other two classes of particles. During the no-current phase, chemical equilibrium must be attained, requiring a uniform lithium distribution among all the particles in a solid-solution active material [30]. Hence, small particles exchange lithium ions, which deintercalate from the particle surface to the (infinitely fast) electrolyte, which intercalate in larger particles in order to attain a uniform chemical potential. Such lithium-ion exchange can also be viewed as the oxidation of small particles, which have a smaller equilibrium electric potential given the higher surface SoL (see equation (10)), driven by the reduction of larger particles having a higher equilibrium potential. In both explanations, lithium ions and electrons are assumed to move freely in the electrolyte and electron-conducting phases, respectively, with no significant transport resistance, enabling what can be regarded as an internal galvanic corrosion process [88]. At the end of the open-circuit phase ($t = 20$ min in figure 6(a)), the numerical simulation shows that the three particle classes have reached an almost uniform SoL distribution (notably, a uniform distribution at $\tilde{c} = 0.2$ would be obtained if a longer relaxation period were allowed). The following current pulse

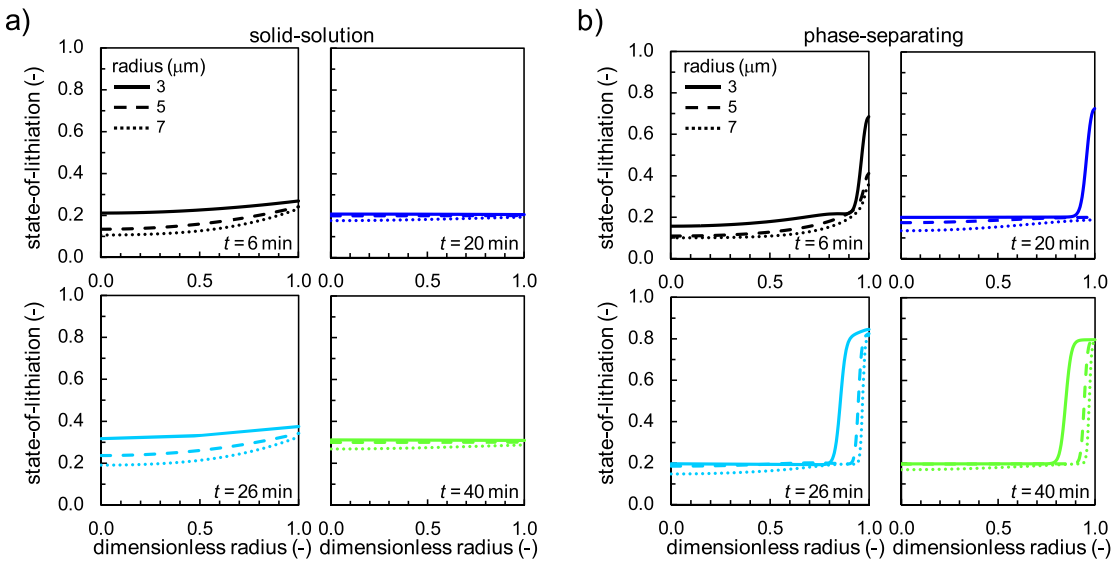

Figure 6. SoL distribution along the dimensionless radii of particles at the end of current pulses ($t = 6$ min and $t = 26$ min) and of open-circuit phases ($t = 20$ min and $t = 40$ min) in an electrode with three particle sizes ($R_1 = 3$ μm, $R_2 = 5$ μm, $R_3 = 7$ μm) with 10/80/10% volumetric composition: (a) solid-solution active material, (b) phase-separating active material. Supplementary videos S5 and S6 report complete animations of these snapshots.

($t = 26$ min) and relaxation ($t = 40$ min) display a similar pattern as highlighted by figure 6(a) and, even more clearly, by supplementary video S5.

The dynamic lithium distribution in a phase-separating active material is reported in figure 6(b). Similar to the solid-solution material, during the current pulse small particles experience more lithiation due to their higher surface-to-volume ratio, as shown at the end of the first current pulse at $t = 6$ min in figure 6(b). However, a different behaviour emerges during the open-circuit phase. In fact, figure 6(b) at $t = 6$ min displays that the phase separation has been triggered in smaller particles, as denoted by the sharp lithium distribution (solid line); conversely, particles with radii $R_2 = 5$ μm (dashed line) and $R_3 = 7$ μm (dotted line) lie mostly within the solid-solution region of their phase diagram at a lithium concentration smaller than the Li-poor composition (i.e. at $\tilde{c} < 0.2$), except for a tiny overshoot at the particle surface which is not sufficient to trigger phase separation in these particles. This is an out-of-equilibrium configuration in a multi-particle system. However, the driving force for inter-particle lithium exchange is basically absent: despite the different SoLs at the particle surface (i.e. $\tilde{c}_i|_{\tilde{r}_i=1}$, which are greater than 0.2 in figure 6(b) at $t = 6$ min), the surface equilibrium potential is the same for all the particles according to the voltage plateau between $\tilde{c} = 0.2$ and $\tilde{c} = 0.8$ for the phase-separating material reported in figure 1(b) (red line). Thus, inter-particle lithium exchange (or, equivalently, internal corrosion with coupled oxidation and reduction in different particles) is marginal if not completely absent in this case, so that only intra-particle chemical equilibration takes place. Such an equilibration towards a uniform chemical potential distribution across each particle is relatively slower than for a solid-solution active material (compare the dotted lines at $t = 20$ min in figures 6(a) and (b)) because the equilibrium potential of a phase-separating active material (and so its chemical potential according to equation (4)) is comparatively flatter (compare blue and red lines in figure 1(b)).

The subsequent pulse repeats the pattern, as also evidenced by the supplementary video S6. During the current pulse, intercalation takes place preferentially in small particles, where the interface separating Li-rich and Li-poor composition shifts inward (solid line at $t = 26$ min). However, lithium intercalation occurs in larger particles too, where phase separation is triggered by nucleation of the Li-rich phase at $\tilde{c} = 0.8$ at particle surface (dashed and dotted lines in figure 6(b)). Upon current interruption, only intra-particle equilibration takes place (compare $t = 26$ min with $t = 40$ min in figure 6(b)) because the presence of the Li-rich phase at the surface of all the three particle classes prevents inter-particle lithium exchange, being the surface equilibrium potential almost the same for all the particles. Thus, despite the different average SoL of the particles, with a more pronounced shrinking-core distribution in small particles, there is no driving force for inter-particle lithium exchange. Such a shrinking-core lithium distribution is a possible metastable, quasi-equilibrium configuration for the electrode, regardless of how much lithium is stored in each particle: the particles do not necessarily need to possess the same average SoL in a multi-particle electrode of phase-separating active material in order to be at electrochemical equilibrium [15, 16].

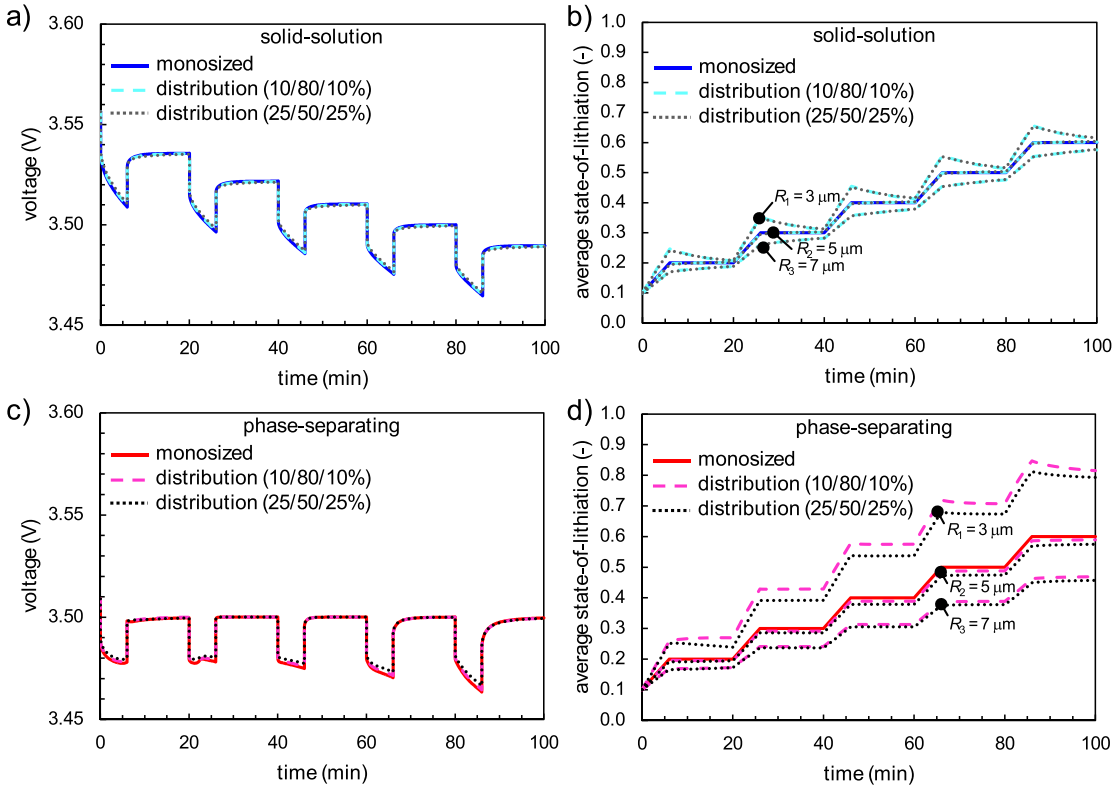

Figure 7. Comparison between the dynamic response of solid-solution and phase-separating active materials for different particle size distributions: monosized (solid lines), 10/80/10% composition (dashed lines), 25/50/25% composition (dotted lines). (a) Electric potential of a solid-solution active material during GITT and (b) corresponding average SoL for each particle class as a function of time. (c) Electric potential of a phase-separating active material during GITT and (d) corresponding average SoL for each particle class as a function of time.

The electrochemical response of solid-solution and phase-separating active materials with particle size distribution is summarised in figure 7. Two symmetric distributions, namely 10/80/10% and 25/50/25%, are compared with the monosized case described in previous sections, with a volume-average particle radius equal to 5 μm in all cases. Figure 7(a) highlights that the electrode potential in a solid-solution active material is basically independent of the particle size distribution in the conditions investigated. Broadly speaking, the electrochemical response of a symmetric particle size distribution is indistinguishable from that of a monosized one even in a dynamic experiment such as pulsed lithiation. This implies that a single equivalent particle radius is sufficient to characterise the electrochemical signature of solid-state diffusion in a solid-solution active material [38]. Nevertheless, despite being inaccessible from the battery terminals, the lithium distribution among the particles is not homogeneous as evidenced in figure 7(b), which reports the average SoL of each particle class as a function of time. As already discussed above, the simulations show that small particles ($R_1 = 3$ μm) lithiate more and faster than large particles ($R_3 = 7$ μm) during current pulses (see also supplementary videos S5 and S7 for 10/80/10% and 25/50/25% compositions, respectively). However, during the open-circuit relaxation phases, inter-particle lithium exchange occurs, with small particles that provide lithium ions to large particles to attain a uniform SoL across the whole electrode (see the converging lines in figure 7(b) during rests). Although such a lithium redistribution does not produce any detectable electrochemical signatures in these conditions, it is reasonable to expect that a wider difference in particle radii and a skewed volumetric distribution should retard the homogenisation of intercalated lithium; this is expected to increase the characteristic time of voltage relaxation, as the large particles are comparatively slower to equilibrate [38].

Moving now to the phase-separating active material, figure 7(c) shows that the electric potential response is only marginally affected by particle size dispersion since only the 25/50/25% composition (dotted line) displays a minor deviation from the 10/80/10% and monosized cases (dashed and solid lines, respectively), which are basically equivalent. However, despite their similarities at battery terminals, tremendous differences are hidden in the lithium distribution among the particles, illustrated in figure 7(d) and in supplementary videos S6 and S8. Let us restrict the comparison between the monosized (solid red line) and 10/80/10% distribution (dashed purple lines) cases. In the latter, small particles ($R_1 = 3$ μm) lithiate more and faster than large particles ($R_3 = 7$ μm) during current pulses, similar to what already described for

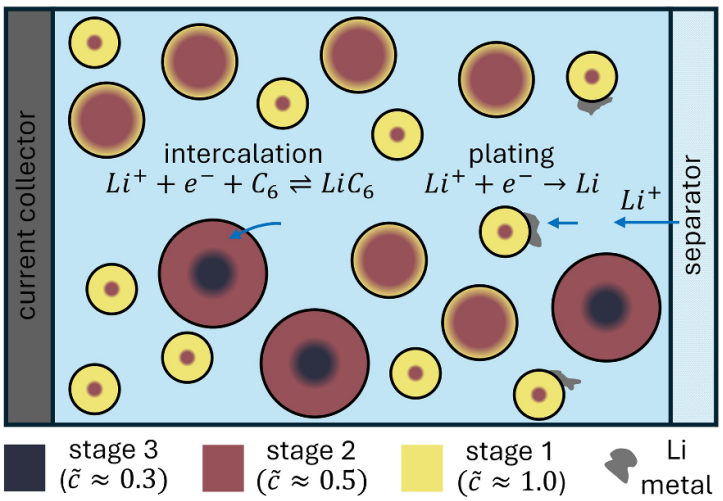

Figure 8. Schematic illustration of lithium plating risk in a graphite negative electrode during fast-charging: while lithiation in large particles lags at stages 2 and 3 (red and dark blue, respectively), small particles may undergo over-lithiation with nucleation of stage 1 (gold) at the surface, where lithium plating may preferentially occur instead of lithium-ion intercalation.

solid-solution active materials. However, the behaviour during open-circuit phases is remarkably different: the average SoL of each particle class remains practically constant, denoting that only minimal inter-particle lithium exchange occurs at rest. This is a consequence of what is described in figure 6(b): the nucleation of the Li-rich phase at the particle surface generates a shrinking-core lithium distribution within the particles, which is a possible quasi-equilibrium configuration in a multi-particle system. Even if the average SoL is different for small and large particles, there is no electrochemical driving force at the particle surfaces to homogenise the lithium content because the Li-rich phase, present at each particle surface, dictates a uniform equilibrium potential for all the particles. Thus, at each current pulse, small particles intercalate more lithium than large particles (compare $R_1 = 3$ μm and $R_3 = 7$ μm in figure 7(d)), which do not homogenise the lithium inventory upon current interruption, so that a wider gap in SoL between small and large particles builds progressively up during pulsed lithiation. These results denote that, as long as the electrode is made of small and large particles, regardless of their volumetric composition, a single particle radius (solid red line) may be representative of the electrode electric response (figure 7(c)), but it turns out to be totally insufficient to capture such a diverging heterogeneous distribution of intercalated lithium among different particles (figure 7(d)). Looking at this result from another perspective, the negligible sensitivity of the electric potential response to the particle size distribution (figure 7(c)) indicates that electrochemical tests cannot effectively detect any heterogeneous distribution of intercalated lithium at electrode level. Notably, albeit not shown for the sake of conciseness, these general features hold also in the case of larger current densities and non-linear charge-transfer kinetics (e.g. Butler–Volmer kinetics instead of equation (6)).

Such observations open relevant practical implications for the dynamic operation of batteries with solid-solution or phase-separating active materials. Take the example of graphite, the most common active material at the negative electrode in Li-ion batteries [2, 4]. Graphite is a phase-separating active material with multiple stable phases, called stages [10, 89], at different degrees of filling: stage 1 ($\tilde{c} \approx 1$), stage 2 ($\tilde{c} \approx 0.5$), stage 3 ($\tilde{c} \approx 0.3$) [87, 90]. In particular, the equilibrium potential of stage 1 is relatively close to 0 mV vs Li metal and, in fact, it has been observed that lithium plating preferentially nucleates on graphite particles at stage 1 [78, 88]. According to what is described above, small particles lithiate faster than large ones due to the higher surface-to-volume ratio, thus leading to over-lithiation with nucleation of stage 1 at the particle surface. In such a scenario, prolonging the charge may likely trigger lithium plating on the surface of small particles, as schematically represented in figure 8, despite the majority of active material volume is still at much lower SoL values.

The situation is not expected to change in the case of a multi-step pulse charging protocol [91, 92]. In multi-step pulse charging, the short rest periods between the current pulses are specifically meant to reduce the concentration polarisation and avoid low electric potentials in graphite, which makes it prone to lithium plating [91]. Nonetheless, according to the model predictions in figure 7(d) for a phase-separating active material with particle size dispersion, such short rest periods may be ineffective because the over-lithiated small particles may not necessarily relax towards lower SoLs. Rest periods must be properly calibrated to enable inter-particle lithium exchange, which is possible only when the electrode is globally in an

out-of-equilibrium configuration. As shown by Lu *et al* [48], placing a rest period during fast-charging when the negative electrode is globally at SoL ≈ 0.45 (that is, in an out-of-equilibrium configuration for stage 1 stability) activates inter-particle lithium exchange, from small particles where stage 1 might have already nucleated to large particles at lower SoL values. This strategy effectively reduces the heterogeneous distribution of intercalated lithium, which would not be smoothed otherwise, and delays the onset of lithium plating once the current is restored to continue the charging [48]. In principle, including a calibrated rest may even reduce the total charging time because, as the plating risk is minimised, comparatively larger currents can be adopted at the end of the charge, thus leading to the motto 'resting for being faster' [48].

4. Conclusions

This study presented a side-by-side comparison of solid-solution and phase-separating active materials with respect to their electrochemical diffusion signatures in dynamic conditions, with implications for characterisation techniques such as GITT as well as for pulse fast-charging. A multi-particle phase-field model was developed by encompassing the minimum number of relevant phenomena (namely, solid-state diffusion and linear intercalation kinetics) to avoid blurring effects in the electrochemical response as well as to promote easy access to modelling and results interpretation for experimentalists and electrochemistry beginners.

During current pulses, lithium intercalation takes place at the particle surface and generates a concentration gradient across the particle radius. For solid-solution active materials, simulations showed that the electrochemical response is dictated by how sensitive the equilibrium potential is to the surface SoL, with the highest sensitivity at the extremes of the SoL window, whose resulting wide electric potential span during open-circuit relaxation must not be interpreted as a consequence of slower solid-state diffusion. The Weppner and Huggins method [20] was shown to generally underestimate solid-state diffusivity in porous electrodes, suggesting that cross-validation with alternative approaches should also be considered.

In a phase-separating active material, pulsed lithiation results in a shrinking-core lithium distribution, with nucleation of the Li-rich phase at the particle surface while the core of the particle remains at a Li-poor composition. Thus, only the potential and diffusion properties of the phase nucleated at the particle surface can be electrochemically probed, so that GITT must be repeated for lithiation and delithiation directions to characterise the Li-rich and Li-poor phases, respectively. Current pulses only shift the Li-rich/Li-poor interface inward by establishing a minor concentration gradient at the particle surface, which quickly relaxes as the current is removed, resulting in a faster electric potential relaxation compared to a solid-solution active material. In general, the electrochemical response within the miscibility gap of a phase-separating active material is the convolution of the kinetic and diffusion properties of the phase nucleated at the particle surface along with the dynamics of the Li-rich/Li-poor interface.

The presence of a particle size distribution creates a distinction between the electrochemical response of active materials and the actual lithium distribution among the particles. In general, small particles lithiate faster and to a greater extent than larger particles in both classes of active materials during current pulses. Upon current interruption, however, different dynamics were revealed. In solid-solution materials, equilibration towards a uniform lithium concentration drives inter-particle lithium exchange from small particles to large particles, which get internally oxidised and reduced, respectively. Such lithium redistribution does not produce any detectable electrochemical signature for a symmetric particle size distribution, so that a single equivalent particle radius is sufficient to characterise the electrochemical signature of solid-state diffusion in a solid-solution material. In a phase-separating active material, instead, the shrinking-core distribution created during current pulses represents a quasi-equilibrium condition which impedes any inter-particle lithium exchange. This implies that, pulse after pulse, the gap between the average SoL between small and large particles continues to increase. Such an inhomogeneous lithium distribution poses some limitations. On the one hand, it reveals that modelling a phase-separating active materials with a single particle radius may be sufficient to reproduce its electrode potential response, while being totally inappropriate to capture the diverging heterogeneous distribution of intercalated lithium in different particles. On the other hand, rest periods, as used in pulse fast-charging, may be ineffective in reducing concentration gradients, unless specifically calibrated. The over-lithiation of small particles can be restrained by applying rest periods when the active material is globally in an out-of-equilibrium configuration in order to activate inter-particle lithium exchange. In fact, Lu *et al* [48] proved that, when charging a 20 Ah m^{-2} graphite electrode up to 3C, a 3 min rest at the electrode SoL ≈ 0.45 (i.e. before that stage 1 becomes thermodynamically stable) can delay the onset of lithium plating beyond 70% SoL compared to ca. 60% SoL when no rest is applied.

In summary, the physics-based analysis of the dynamic behaviour of active materials, taking into account their analogies and differences rooted in materials thermodynamics and electrode morphologies, reveals how

characterisation experiments (such as GITT) must be interpreted and what can and cannot be observed electrochemically at battery terminals. The fundamental insights into the internal processes occurring within active material particles set the foundations for guiding the design and operation of more efficient and resilient Li-ion batteries. Future work will build upon the present investigation by systematically including additional phenomena (i.e. intercalation kinetics, mechanical effects and electrolyte transport) in order to assess their interplay and their specific contribution to the dynamic electrochemical behaviour of battery materials.

Data availability statement

All data that support the findings of this study are included within the article (and any supplementary files).

Acknowledgments

This study received funding from the European Union—Next Generation EU—National Recovery and Resilience Plan (NRRP)—MISSION 4 Component 1, INVESTMENT N. 1.1, call PRIN 2022 D.D. 104 02-02-2022—CUP N. I53D23001550006, within the project 'Integrated procedures for FAST ChARging with online state-of-health evaluation of lithium-ion batteries (FASTCAR)'. M.L. acknowledges funding from the European Union NextGeneration EU—National Recovery and Resilience Plan (NRRP)—MISSION 4 Component 2, INVESTMENT N. 1.3—CUP N. I53C22001450006, within the Project 'Network 4 Energy Sustainable Transition (NEST)'. This manuscript reflects only the authors' views and opinions, neither the European Union nor the European Commission can be considered responsible for them.

Author contributions

Marco Lagnoni 0000-0001-6715-3317
Conceptualization (supporting), Formal analysis (equal), Investigation (equal), Methodology (supporting), Software (equal), Writing – original draft (equal), Writing – review & editing (equal)

Antonio Bertei 0000-0002-3202-6825
Conceptualization (lead), Formal analysis (equal), Funding acquisition (lead), Investigation (equal), Methodology (lead), Software (equal), Writing – original draft (equal), Writing – review & editing (equal)

References

[1] Masias A, Marcicki J and Paxton W A 2021 Opportunities and challenges of lithium ion batteries in automotive applications *ACS Energy Lett.* **6** 621–30
[2] Kim T, Song W, Son D-Y, Ono L K and Qi Y 2019 Lithium-ion batteries: outlook on present, future, and hybridized technologies *J. Mater. Chem. A* **7** 2942–64
[3] Scrosati B 1992 Lithium rocking chair batteries: an old concept? *J. Electrochem. Soc.* **139** 2776–81
[4] Woehrle T 2018 Lithium-ion cell *Lithium-Ion Batteries: Basics and Applications* ed R Korthauer (Springer) pp 101–11
[5] Liu Z, Yu A and Lee J Y 1999 Synthesis and characterization of $LiNi_{1-x-y}Co_xMn_yO_2$ as the cathode materials of secondary lithium batteries *J. Power Sources* **81–82** 416–9
[6] Nitta N, Wu F, Lee J T and Yushin G 2015 Li-ion battery materials: present and future *Mater. Today* **18** 252–64
[7] Kraft L, Zünd T, Schreiner D, Wilhelm R, Günter F J, Reinhart G, Gasteiger H A and Jossen A 2021 Comparative evaluation of LMR-NCM and NCA cathode active materials in multilayer lithium-ion pouch cells: part II. Rate capability, long-term stability, and thermal behavior *J. Electrochem. Soc.* **168** 020537
[8] Padhi A K, Nanjundaswamy K S and Goodenough J B 1997 Phospho-olivines as positive-electrode materials for rechargeable lithium batteries *J. Electrochem. Soc.* **144** 1188–94
[9] Kang B and Ceder G 2009 Battery materials for ultrafast charging and discharging *Nature* **458** 190–3
[10] Asenbauer J, Eisenmann T, Kuenzel M, Kazzazi A, Chen Z and Bresser D 2020 The success story of graphite as a lithium-ion anode material—fundamentals, remaining challenges, and recent developments including silicon (oxide) composites *Sustain. Energy Fuels* **4** 5387–416
[11] Rodrigues M-T F, Gilbert J A, Kalaga K and Abraham D P 2020 Insights on the cycling behavior of a highly-prelithiated silicon–graphite electrode in lithium-ion cells *J. Phys.* **2** 024002
[12] Choi J W and Aurbach D 2016 Promise and reality of post-lithium-ion batteries with high energy densities *Nat. Rev. Mater.* **1** 16013
[13] Lee J K, Oh C, Kim N, Hwang J-Y and Sun Y-K 2016 Rational design of silicon-based composites for high-energy storage devices *J. Mater. Chem. A* **4** 5366–84
[14] Lagnoni M, Armiento G, Nicolella C and Bertei A 2024 Intercalation in Li-ion batteries: thermodynamics and its relation to non-ideal solid-state diffusion *Prog. Energy* **6** 023002
[15] Smith R B and Bazant M Z 2017 Multiphase porous electrode theory *J. Electrochem. Soc.* **164** E3291–310
[16] Dreyer W, Guhlke C and Huth R 2011 The behavior of a many-particle electrode in a lithium-ion battery *Physica D* **240** 1008–19
[17] Lai W and Ciucci F 2010 Thermodynamics and kinetics of phase transformation in intercalation battery electrodes—phenomenological modeling *Electrochim. Acta* **56** 531–42
[18] Ferguson T R and Bazant M Z 2012 Nonequilibrium thermodynamics of porous electrodes *J. Electrochem. Soc.* **159** A1967–85

[19] Lamorgese A G, Molin D and Mauri R 2011 Phase field approach to multiphase flow modeling *Milan J. Math.* **79** 597–642
[20] Weppner W and Huggins R A 1977 Determination of the kinetic parameters of mixed-conducting electrodes and application to the system Li_3Sb *J. Electrochem. Soc.* **124** 1569–78
[21] Dees D W, Kawauchi S, Abraham D P and Prakash J 2009 Analysis of the galvanostatic intermittent titration technique (GITT) as applied to a lithium-ion porous electrode *J. Power Sources* **189** 263–8
[22] Chien Y C, Liu H, Menon A S, Brant W R, Brandell D and Lacey M J 2023 Rapid determination of solid-state diffusion coefficients in Li-based batteries via intermittent current interruption method *Nat. Commun.* **14** 2289
[23] Kang S D and Chueh W C 2021 Galvanostatic intermittent titration technique reinvented: part I. A critical review *J. Electrochem. Soc.* **168** 120504
[24] Nickol A, Schied T, Heubner C, Schneider M, Michaelis A, Bobeth M and Cuniberti G 2020 GITT analysis of lithium insertion cathodes for determining the lithium diffusion coefficient at low temperature: challenges and pitfalls *J. Electrochem. Soc.* **167** 090546
[25] Lee H, Yang S, Kim S, Song J, Park J, Doh C-H, Ha Y-C, Kwon T-S and Lee Y M 2022 Understanding the effects of diffusion coefficient and exchange current density on the electrochemical model of lithium-ion batteries *Curr. Opin. Electrochem.* **34** 100986
[26] Deng H D, Jin N, Attia P M, Lim K, Kang S D, Kapate N, Zhao H, Li Y, Bazant M Z and Chueh W C 2024 Beyond constant current: origin of pulse-induced activation in phase-transforming battery electrodes *ACS Nano* **18** 2210–8
[27] Geslin A, Xu L, Ganapathi D, Moy K, Chueh W C and Onori S 2024 Dynamic cycling enhances battery lifetime *Nat. Energy* **10** 172–80
[28] Zhou Y *et al* 2016 High-rate charging induced intermediate phases and structural changes of layer-structured cathode for lithium-ion batteries *Adv. Energy Mater.* **6** 1600597
[29] Grenier A, Liu H, Wiaderek K M, Lebens-Higgins Z W, Borkiewicz O J, Piper L F J, Chupas P J and Chapman K W 2017 Reaction heterogeneity in $LiNi_{0.8}Co_{0.15}Al_{0.05}O_2$ induced by surface layer *Chem. Mater.* **29** 7345–52
[30] Park J *et al* 2021 Fictitious phase separation in Li layered oxides driven by electro-autocatalysis *Nat. Mater.* **20** 991–9
[31] Cogswell D A and Bazant M Z 2012 Coherency strain and the kinetics of phase separation in $LiFePO_4$ nanoparticles *ACS Nano* **6** 2215–25
[32] Bai P, Cogswell D A and Bazant M Z 2011 Suppression of phase separation in $LiFePO_4$ nanoparticles during battery discharge *Nano Lett.* **11** 4890–6
[33] Morgan L M *et al* 2022 From atoms to cells: multiscale modeling of $LiNi_xMn_yCo_zO_2$ cathodes for li-ion batteries *ACS Energy Lett.* **7** 108–22
[34] Brosa Planella F *et al* 2022 A continuum of physics-based lithium-ion battery models reviewed *Prog. Energy* **4** 042003
[35] Van der Ven A and Ceder G 2001 Lithium diffusion mechanisms in layered intercalation compounds *J. Power Sources* **97–98** 529–31
[36] Cen J, Zhu B and Scanlon D O 2023 Exploring battery cathode materials in the Li-Ni-O phase diagrams using structure prediction *J. Phys. Energy* **5** 035005
[37] Shah K *et al* 2017 State of the art and future research needs for multiscale analysis of Li-ion cells *J. Electrochem. Energy Convers. Storage* **14** 020801
[38] Horner J S, Whang G, Ashby D S, Kolesnichenko I V, Lambert T N, Dunn B S, Talin A A and Roberts S A 2021 Electrochemical modeling of GITT measurements for improved solid-state diffusion coefficient evaluation *ACS Appl. Energy Mater.* **4** 11460–9
[39] Han B C, Van der Ven A, Morgan D and Ceder G 2004 Electrochemical modeling of intercalation processes with phase field models *Electrochim. Acta* **49** 4691–9
[40] Markevich E, Levi M D and Aurbach D 2005 Comparison between potentiostatic and galvanostatic intermittent titration techniques for determination of chemical diffusion coefficients in ion-insertion electrodes *J. Electroanal. Chem.* **580** 231–7
[41] Ciucci F and Lai W 2012 Electrochemical impedance spectroscopy of phase transition materials *Electrochim. Acta* **81** 205–16
[42] Bazant M Z 2013 Theory of chemical kinetics and charge transfer based on nonequilibrium thermodynamics *Acc. Chem. Res.* **46** 1144–60
[43] Fraggedakis D, McEldrew M, Smith R B, Krishnan Y, Zhang Y, Bai P, Chueh W C, Shao-Horn Y and Bazant M Z 2021 Theory of coupled ion-electron transfer kinetics *Electrochim. Acta* **367** 137432
[44] Smith R B, Khoo E and Bazant M Z 2017 Intercalation kinetics in multiphase-layered materials *J. Phys. Chem. C* **121** 12505–23
[45] Bazant M Z 2017 Thermodynamic stability of driven open systems and control of phase separation by electro-autocatalysis *Faraday Discuss.* **199** 423–63
[46] Koo B *et al* 2023 Dynamic surface phases controlling asymmetry of high-rate lithiation and delithiation in phase-separating electrodes *Energy Environ. Sci.* **16** 3302–13
[47] Zhao H *et al* 2023 Learning heterogeneous reaction kinetics from x-ray videos pixel by pixel *Nature* **621** 289–94
[48] Lu X *et al* 2023 Multiscale dynamics of charging and plating in graphite electrodes coupling operando microscopy and phase-field modelling *Nat. Commun.* **14** 5127
[49] Pandurangi S S, Hall D S, Grey C P, Deshpande V S and Fleck N A 2023 Chemo-mechanical analysis of lithiation/delithiation of Ni-rich single crystals *J. Electrochem. Soc.* **170** 050531
[50] Mohtat P, Lee S, Sulzer V, Siegel J B and Stefanopoulou A G 2020 Differential expansion and voltage model for Li-ion batteries at practical charging rates *J. Electrochem. Soc.* **167** 110561
[51] Lee J and Kim C 2021 Effective modulus of Si electrodes considering Li concentration, volume expansion, pore, and Poisson's ratio of Li-ion batteries *J. Mech. Sci. Technol.* **35** 2115–21
[52] Latz A and Zausch J 2011 Thermodynamic consistent transport theory of Li-ion batteries *J. Power Sources* **196** 3296–302
[53] Bizeray A M, Howey D A and Monroe C W 2016 Resolving a discrepancy in diffusion potentials, with a case study for Li-Ion batteries *J. Electrochem. Soc.* **163** E223–9
[54] Lagnoni M, Nicolella C and Bertei A 2022 Comparison of electrolyte transport modelling in lithium-ion batteries: concentrated solution theory vs generalized Nernst–Planck model *J. Electrochem. Soc.* **169** 020570
[55] Lai W and Ciucci F 2011 Mathematical modeling of porous battery electrodes—revisit of Newman's model *Electrochim. Acta* **56** 4369–77
[56] Lagnoni M, Scarpelli C, Lutzemberger G and Bertei A 2024 Critical comparison of equivalent circuit and physics-based models for lithium-ion batteries: a graphite/lithium-iron-phosphate case study *J. Energy Storage* **94** 112326
[57] Bertei A, Lamorgese A and Mauri R 2020 Constitutive relations of thermal and mass diffusion *J. Non-Equilib. Thermodyn.* **45** 27–38
[58] Cahn J W and Hilliard J E 1958 Free energy of a nonuniform system. I Interfacial free energy *J. Chem. Phys.* **28** 258–67
[59] Daubner S, Weichel M, Schneider D and Nestler B 2022 Modeling intercalation in cathode materials with phase-field methods: assumptions and implications using the example of $LiFePO_4$ *Electrochim. Acta* **421** 140516
[60] Hildebrand J H 1951 The term 'regular solution' *Nature* **168** 868

[61] Singh G K, Ceder G and Bazant M Z 2008 Intercalation dynamics in rechargeable battery materials: general theory and phase-transformation waves in $LiFePO_4$ *Electrochim. Acta* **53** 7599–613
[62] Bard A J and Faulkner L R 2001 *Electrochemical Methods: Fundamentals and Applications* (Wiley)
[63] Lu X *et al* 2020 3D microstructure design of lithium-ion battery electrodes assisted by x-ray nano-computed tomography and modelling *Nat. Commun.* **11** 2079
[64] Bazant M Z 2023 Unified quantum theory of electrochemical kinetics by coupled ion–electron transfer *Faraday Discuss.* **246** 60–124
[65] Ahn S *et al* 2023 Chemical origins of a fast-charge performance in disordered carbon anodes *ACS Appl. Energy Mater.* **6** 8455–65
[66] Wagemaker M, Singh D P, Borghols W J H, Lafont U, Haverkate L, Peterson V K and Mulder F M 2011 Dynamic solubility limits in nanosized olivine $LiFePO_4$ *J. Am. Chem. Soc.* **133** 10222–8
[67] Nguyen T-T, Delobel B, Berthe M, Fleutot B, Demortière A and Delacourt C 2022 Mathematical modeling of energy-dense NMC electrodes: I. Determination of input parameters *J. Electrochem. Soc.* **169** 040546
[68] Lagnoni M, Nicolella C and Bertei A 2021 Survey and sensitivity analysis of critical parameters in lithium-ion battery thermo-electrochemical modeling *Electrochim. Acta* **394** 139098
[69] Marcato A, Santos J E, Liu C, Boccardo G, Marchisio D and Franco A A 2023 Modeling the 4D discharge of lithium-ion batteries with a multiscale time-dependent deep learning framework *Energy Storage Mater.* **63** 102927
[70] Kench S, Squires I, Dahari A, Brosa Planella F, Roberts S A and Cooper S J 2024 Li-ion battery design through microstructural optimization using generative AI *Matter* **7** 4260–9
[71] Xu C, Merryweather A J, Pandurangi S S, Lun Z, Hall D S, Deshpande V S, Fleck N A, Schnedermann C, Rao A and Grey C P 2022 Operando visualization of kinetically induced lithium heterogeneities in single-particle layered Ni-rich cathodes *Joule* **6** 2535–46
[72] Fraggedakis D, Nadkarni N, Gao T, Zhou T, Zhang Y, Han Y, Stephens R M, Shao-Horn Y and Bazant M Z 2020 A scaling law to determine phase morphologies during ion intercalation *Energy Environ. Sci.* **13** 2142–52
[73] Lee S W, McDowell M T, Choi J W and Cui Y 2011 Anomalous shape changes of silicon nanopillars by electrochemical lithiation *Nano Lett.* **11** 3034–9
[74] Xu J, Paredes-Goyes B, Su Z, Scheel M, Weitkamp T, Demortière A and Franco A A 2023 Computational model for predicting particle fracture during electrode calendering *Batter Supercaps* **6** e202300371
[75] Edge J S *et al* 2021 Lithium ion battery degradation: what you need to know *Phys. Chem. Chem. Phys.* **23** 8200–21
[76] Single F, Horstmann B and Latz A 2016 Dynamics and morphology of solid electrolyte interphase (SEI) *Phys. Chem. Chem. Phys.* **18** 17810–4
[77] von Kolzenberg L, Latz A and Horstmann B 2020 Solid–electrolyte interphase during battery cycling: theory of growth regimes *ChemSusChem* **13** 3901–10
[78] Gao T, Han Y, Fraggedakis D, Das S, Zhou T, Yeh C-N, Xu S, Chueh W C, Li J and Bazant M Z 2021 Interplay of lithium intercalation and plating on a single graphite particle *Joule* **5** 393–414
[79] Lian H and Bazant M Z 2024 Modeling lithium plating onset on porous graphite electrodes under fast charging with hierarchical multiphase porous electrode theory *J. Electrochem. Soc.* **171** 010526
[80] Barzacchi L, Lagnoni M, Di Rienzo R, Bertei A and Baronti F 2022 Enabling early detection of lithium-ion battery degradation by linking electrochemical properties to equivalent circuit model parameters *J. Energy Storage* **50** 104213
[81] Bessler W G 2007 Rapid impedance modeling via potential step and current relaxation simulations *J. Electrochem. Soc.* **154** B1186
[82] Huang J D, Meisel C, Sullivan N P, Zakutayev A and O'Hayre R 2024 Rapid mapping of electrochemical processes in energy-conversion devices *Joule* **8** 2049–72
[83] Kang S D, Kuo J J, Kapate N, Hong J, Park J and Chueh W C 2021 Galvanostatic intermittent titration technique reinvented: part II. experiments *J. Electrochem. Soc.* **168** 120503
[84] Colclasure A M and Kee R J 2010 Thermodynamically consistent modeling of elementary electrochemistry in lithium-ion batteries *Electrochim. Acta* **55** 8960–73
[85] Deiss E 2005 Spurious chemical diffusion coefficients of Li^+ in electrode materials evaluated with GITT *Electrochim. Acta* **50** 2927–32
[86] Zhu Y and Wang C 2010 Galvanostatic intermittent titration technique for phase-transformation electrodes *J. Phys. Chem. C* **114** 2830–41
[87] Thomas-Alyea K E, Jung C, Smith R B and Bazant M Z 2017 *In situ* observation and mathematical modeling of lithium distribution within graphite *J. Electrochem. Soc.* **164** E3063–72
[88] Chen Y, Chen K-H, Sanchez A J, Kazyak E, Goel V, Gorlin Y, Christensen J, Thornton K and Dasgupta N P 2021 Operando video microscopy of Li plating and re-intercalation on graphite anodes during fast charging *J. Mater. Chem. A* **9** 23522–36
[89] Zhang H, Yang Y, Ren D, Wang L and He X 2021 Graphite as anode materials: fundamental mechanism, recent progress and advances *Energy Storage Mater.* **36** 147–70
[90] Guo Y, Smith R B, Yu Z, Efetov D K, Wang J, Kim P, Bazant M Z and Brus L E 2016 Li intercalation into graphite: direct optical imaging and Cahn–Hilliard reaction dynamics *J. Phys. Chem. Lett.* **7** 2151–6
[91] Tomaszewska A *et al* 2019 Lithium-ion battery fast charging: a review *eTransportation* **1** 100011
[92] Adam A, Wandt J, Knobbe E, Bauer G and Kwade A 2020 Fast-charging of automotive lithium-ion cells: *in-situ* lithium-plating detection and comparison of different cell designs *J. Electrochem. Soc.* **167** 130503